

An approach for predicting multi-support seismic underground motions in layered saturated soil under surface water



Guohuan Liu^{a,b}, Haitao Yu^{c,*}, Yaqiang Liu^b, Jijian Lian^a

^a State Key Laboratory of Hydraulic Engineering Simulation and Safety, Tianjin University, Tianjin, China

^b School of Civil Engineering, Tianjin University, Tianjin, China

^c Key Laboratory of Geotechnical and Underground Engineering of Ministry of Education, Tongji University, Shanghai 200092, China

ARTICLE INFO

Keywords:

Saturated soil under surface water
Multi-support seismic motions
Transfer function
Power spectral density
Cross-coherence function

ABSTRACT

Simulation of multi-support (i.e. spatially variable) seismic underground motions in sea areas plays a significant role in the seismic analysis of cross-sea structures such as cross-sea bridges or subsea tunnels. However, existing approaches for predicting multi-support seismic motions mainly focus on the dry site soils without overlying surface water. This paper proposes an approach for predicting multi-support seismic underground motions in layered saturated half space under surface water, subjected to oblique incident *P* waves. The transfer function in saturated soil under surface water, as the theoretical basis of the subsequent numerical simulation, is first derived based on wave propagation theory and the calculated reflection coefficients of *P* wave-induced *P1*, *P2*, *SV* waves in saturated soils. The derived transfer function is further employed to deduce and obtain the underground (sub-seabed) power spectral density function and response spectrum function. The two obtained functions, combined with the additional cross-coherence function, are subsequently employed to construct the cross power spectral density matrix and thus to simulate multi-support seismic underground motions. The solutions are validated against the target power spectral density, target response spectrum and target cross-coherence functions. A parametric analysis is presented where the effects of the soil thickness, the incident angle and the overlying water depth are investigated. Results show that the soil thickness, incident angle and overlying water depth have significant influences on the amplitude of transfer functions, which further affect the ratios between seismic ground and underground motions.

1. Introduction

Various components including wave scattering, wave passage, and site simplification effects cause the ground motion to vary spatially [1,10,12,21,39,9]. It has been observed that the spatial variation of seismic motions has significant influence on the dynamic response of engineering structures, especially for those structures such as long-span bridges, transmission tower-lines systems, tunnels and dams [2,41–44]. Therefore, the reasonable simulations and predictions of multi-support seismic motions are necessary for a reliable structural response analysis [21,23,3,33,46].

Generally, it is necessary for simulating the multi-support seismic motions to construct the cross power spectral density matrix, which need the target PSD (power spectral density) function, target response spectrum and coherence function [20,22,24,27,31,35]. Based on this research framework, a number of methods have been developed, proposed and employed. In particular, Deodatis [15] presented a method

to simulate spatial ground motions with different power spectral densities at different locations and investigated the influence of the spatial variation of ground motions on the seismic response of large embankment dams. This method was then extended to generate spatially varying seismic ground motion time histories by Deodatis et al. [16]. Considering the influence of layered irregular sites and random soil properties on coherence functions, [4,5] presented an approximate method to simulate the spatially varying ground motions on the surface of non-uniform sites. Their method was then paid close attention and was extensively developed by many researchers [26,28,45]. Furthermore, the impact of the spatially varying seismic motions on the seismic response of different types of structures, such as transmission tower-lines, large dams and large-span bridges, were also investigated by [1,37,14,30,48,19,34].

Current researches on the multi-support seismic motions mainly focus on the seismic response in the dry soil sites without overlying surface water [49,50]. However, for those long-span cross-sea

* Corresponding author.

E-mail address: yuhaitao@tongji.edu.cn (H. Yu).

structures, such as cross-sea bridges and subsea tunnels, the site soils (or sub-seabed) are saturated and overlain by the surface water. Thus, the theoretical models or functions that are applicable to simulate seismic motions in dry soil are not appropriate. Therefore, it is very necessary to investigate the specific theoretical functions that are applicable to predict multi-support seismic motions in saturated soils with overlying surface water. Based on the Biot theory [6–8], researchers extensively investigated the wave propagation in the saturated soils and further emphases were given to the investigation on the complex reflection and refraction in saturated solid and at medium-fluid interface. Such representative works include [18,17,32,11,47,40], etc. In addition, [38] particularly investigated the effects of random variations of soil properties on site amplification of seismic waves considering soil saturation, considered as a development of the study on seismic motions in saturated soils, despite not considering the overlying surface water. Recently, Liu and Liang investigate the approach for simulating the multi-support earthquake underground motions, but the research is only limited to the dry soil without considering the overlying surface water.

This paper focuses on a feasible approach for predicting multi-support seismic motions in the layered saturated soil under surface water, which can be used for the seismic analysis of large-span cross-sea structures. Firstly, the potential functions of saturated elastic-solid media overlying with ideal fluid are deduced and the corresponding transfer functions, the theoretical basis of the subsequent numerical simulation, are derived in this paper. Subsequently, the underground power spectral density (PSD) function and response spectrum function for generating the multi-support seismic underground motions are obtained with the derived transfer functions. Furthermore, the two key functions combined with the additional cross-coherence function are subsequently employed to construct the cross power spectral density matrix and thus to simulate multi-support seismic underground motions. Finally, the multi-support seismic underground motions are simulated and validated against the target functions. In addition, a parametric analysis on the effects of the soil thickness, incident angle and overlying water depth are investigated.

2. Wave equations and transfer function in saturated soil under surface water

First, the theoretical formula of seismic waves in saturated soil with overlying water are deduced. Fig. 1 schematically shows the considered multi-layer saturated soil with overlying surface water. In the figure, H and h_j represent the depth of the overlying water and the thickness of the (j)th layer respectively; ρ_w and K are the density and bulk modulus of the overlying water respectively; ρ_s , ρ_f , μ and ϕ respectively represent the soil density, fluid density, shear modulus, porosity; K_s , K_f , K_b and K_0 denote bulk modulus of the solid, bulk modulus of the fluid, bulk

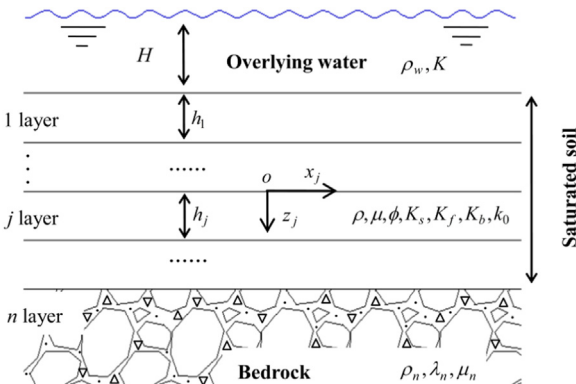


Fig. 1. Schematic diagram of a layered half-space saturated soil with an overlying water layer.

modulus of the solid skeleton and permeability coefficient, respectively; ρ_n is the density of the bedrock and λ_n , μ_n represent Lamé constants respectively.

2.1. Basic theory: potential functions in different media

The governing equations for the displacement of the solid medium and liquid portion of porous skeleton are obtained by taking the effect of dissipation due to flow of the viscous liquid relative to the solid.

According to the Biot porous media theory [6–8], the potential functions of saturated soil can be expressed as

$$\phi_k = E_{Pk} e^{i[\omega t - \delta_k(xw_{k1} - zw_{k3})]} + F_{Pk} e^{i[\omega t - \delta_3(xw_{31} + zw_{33})]}, \quad (k = 1, 2) \quad (1)$$

$$\psi_1 = E_S e^{i[\omega t - \delta_3(xw_{31} - zw_{33})]} + F_S e^{i[\omega t - \delta_3(xw_{31} + zw_{33})]} \quad (2)$$

where ϕ_1 , ϕ_2 and ψ_1 are the potential functions of the P1, P2 and SV waves respectively; E_{P1} , E_{P2} and E_S are the potential amplitudes of the corresponding upward-travelling waves; F_{P1} , F_{P2} and F_S are the potential amplitudes of the corresponding downward-travelling waves; w_{kx} and w_{kz} denote the components of the unit vector in the x-direction and z-direction.

According to Snell's law, the horizontal wave numbers (k_x) of harmonic waves are the same in x-direction

$$k_x = \delta_k w_{kx} = \sin \theta \cdot \omega / c_k, \quad w_{kx} = (\omega / c_k \cdot \sin \theta) / \delta_k, \quad w_{kz} = (1 - w_{kx}^2)^{1/2}, \quad (k = 1, 2, 3) \quad (3a)$$

$$c_k = (M/\rho)^{1/2} / \text{Re}(\Omega_k^{1/2}), \quad (k = 1, 2, 3) \quad (3b)$$

where ω is the circular frequency of the incident wave; θ is the incident angle; c_k are the phase velocity and $k = 1, 2, 3$ denoting the P1, P2, and SV waves respectively; Re denotes the real part of the parameter. For more introduction, the following expressions are given and defined as

$$\rho = \rho_{11} + 2\rho_{12} + \rho_{22} \quad (4a)$$

$$\rho_{11} = (1 - \phi)\rho_s + \phi(\alpha - 1)\rho_f, \quad \rho_{12} = -\phi(\alpha - 1)\rho_f, \quad \rho_{22} = \phi\alpha\rho_f \quad (4b)$$

$$A = (\phi K_b + (1 - \phi)K_f(1 - \phi - K_b/K_s)) / (\phi + K_f/K_s(1 - \phi - K_b/K_s)) - 2\mu/3 \quad (4c)$$

$$Q = \phi K_f(1 - \phi - K_b/K_s) / (\phi + K_f/K_s(1 - \phi - K_b/K_s)) \quad (4d)$$

$$R = \phi^2 K_f / (\phi + K_f/K_s(1 - \phi - K_b/K_s)) \quad (4e)$$

$$N = \mu, \quad P = A + 2N, \quad M = P + R + 2Q \quad (4f)$$

$$\sigma_{11} = P/M, \quad \sigma_{12} = Q/M, \quad \sigma_{22} = R/M, \quad \gamma_{11} = \rho_{11}/\rho, \quad \gamma_{12} = \rho_{12}/\rho, \quad \gamma_{22} = \rho_{22}/\rho \quad (4g)$$

$$E = \sigma_{11}\sigma_{22} - \sigma_{12}^2, \quad F = \gamma_{11}\sigma_{22} + \gamma_{22}\sigma_{11} - 2\gamma_{12}\sigma_{12}, \quad G = \gamma_{11}\gamma_{22} - \gamma_{12}^2 \quad (4h)$$

$$b = \sigma_{12} + \sigma_{22}, \quad g = \gamma_{11}\sigma_{22} - \gamma_{12}\sigma_{12}, \quad h = \gamma_{22}\sigma_{12} - \gamma_{12}\sigma_{22}, \quad f = \eta/\rho\omega \quad (4i)$$

$$\delta_0^2 = \rho\omega^2/M, \quad \Delta^2 = F^2 - 4EG - 2if(F - 2E) - f^2 \quad (4j)$$

$$\Omega_{1,2} = (F - if \mp \Delta)/2E, \quad \Omega_3 = (M/N)(G - if)/(\gamma_{22} - if) \quad (4k)$$

$$\delta_j^2 = \delta_0^2 \Omega_j \quad (j = 1, 2, 3) \quad (4l)$$

In Eq. 4b, $\alpha = 1 + \gamma(1 + \phi)/\varphi$ with γ as the coefficient of the induced inertia on the solid phase (due to the oscillation of solid skeleton in fluid).

The displacements of the solid fluid phase can be expressed by the potential functions as

$$u_x = \frac{\partial \phi_1}{\partial x} + \frac{\partial \phi_2}{\partial x} + \frac{\partial \psi_1}{\partial z}, \quad u_z = \frac{\partial \phi_1}{\partial z} + \frac{\partial \phi_2}{\partial z} - \frac{\partial \psi_1}{\partial x} \quad (5a)$$

$$U_x = \beta_1 \frac{\partial \phi_1}{\partial x} + \beta_2 \frac{\partial \phi_2}{\partial x} + \alpha_0 \frac{\partial \psi_1}{\partial z}, \quad U_z = \beta_1 \frac{\partial \phi_1}{\partial z} + \beta_2 \frac{\partial \phi_2}{\partial z} - \alpha_0 \frac{\partial \psi_1}{\partial x} \quad (5b)$$

According to Eq. (5), the stresses of the solid-fluid phase can be expressed as

$$\sigma_{ij} = \left(Ae + Q\xi \right) \delta_{ij} + 2Ne_{ij}, \quad \tau = -\phi p = Qe + R\xi, \quad e_{ij} = \frac{1}{2} \left(u_{i,j} + u_{j,i} \right) \quad (i, j = 1, 3) \quad (6)$$

where δ_{ij} is Kronecker coefficient; $e = \nabla \cdot u$; $\xi = \nabla \cdot U$; p is pore fluid pressure.

The potential functions of ideal fluid can be expressed as

$$\phi_f = E_{pf} e^{i(\omega t - k_x x - k_{fz} z)} + F_{pf} e^{i(\omega t - k_x x + k_{fz} z)} \quad (7)$$

where the wave numbers of P wave in ideal fluid are $k_f = \omega/c_f$ and $k_{fz} = \sqrt{k_f^2 - k_x^2}$; $c_f = \sqrt{K/\rho_f}$.

The displacements and pressure of fluid can be expressed as

$$U_{xf} = \frac{\partial \phi_f}{\partial x}, \quad U_{zf} = \frac{\partial \phi_f}{\partial z}, \quad p = -\rho_f \frac{\partial^2 \phi_f}{\partial t^2} \quad (8)$$

2.2. Boundary conditions

The boundary conditions of the saturated soil model in Fig. 1 are investigated in this section. The boundary consists of two types, i.e. the interface of soil layers and the interface between saturated soil and overlying water.

At the interface of elastic solid-saturated soil layers, both the displacement and stress continuity should be satisfied, as follows.

(1) The vertical displacement is continuous

$$u_z = u_{zn} \quad (9a)$$

(2) The horizontal displacement is continuous

$$u_x = u_{xn} \quad (9b)$$

(3) The normal stress is continuous

$$\sigma_{zz} + \tau = \sigma_{zzn} \quad (9c)$$

(4) The shear stress is continuous

$$\sigma_{zx} = \sigma_{zxn} \quad (9d)$$

(5) The relative displacement of solid-liquid is zero at the interface of elastic solid-saturated soil

$$u_z = U_z \quad (9e)$$

Due to the fact that the component of P wave disappears in the overlying water, at the interface between saturated soil and overlying water, we have

(1) The vertical displacement is continuous

$$u_z = U_{zf} \quad (10a)$$

(2) The horizontal displacement is continuous

$$u_x = U_{xf} \quad (10b)$$

(3) The normal stress is continuous

$$\sigma_{zz} + \tau = -p \quad (10c)$$

(4) The shear stress is continuous

$$\sigma_{zx} = 0 \quad (10d)$$

(5) The pressure is zero at the free surface of ideal fluid

$$\rho_f \frac{\partial^2 \phi_f}{\partial t^2} = 0 \quad (10e)$$

2.3. Derivation process of transfer matrix

Based on the above analysis, each saturated soil layer has three up-going waves and three down-going waves. The amplitude vector H_n and the stress-displacement vector S_n of the bedrock can be expressed as

$$H_n = (E_{pn}, F_{pn}, E_{sn}, F_{sn})^T, \quad S_n = (u_z, u_x, \sigma_{33}, \sigma_{13})^T \quad (11)$$

$$S_n = T_n H_n \quad (12)$$

where T_n is a matrix of 4×4 , in which each parameter is defined in Appendix A.

According to Eqs. 1 and 2, each saturated soil layer has three upward-travelling waves and three downward-travelling waves. The amplitude vector H_j and stress-displacement vector S_j of the (j)th layer can be expressed as

$$H_j = (E_{pj}, F_{pj}, E_{sj}, F_{sj})^T, \quad (j = 1, 2, 3, \dots, n-1) \quad (13)$$

$$S_j = (u_{zj}, u_{xj}, \sigma_{33j} + \tau_j, \sigma_{13j}, p_j, \phi_j (U_{zj} - u_{zj}))^T, \quad (j = 1, 2, 3, \dots, n-1) \quad (14)$$

Eqs. 13 and 14 can be connected by using the following equation

$$S_j = T_{sj} H_j \quad (15)$$

where T_{sj} can be obtained by substituting Eqs. (1) and (2) into Eqs. (5) and (6), each parameter of T_{sj} is defined in Appendix B.

In the ($j+1$)th layer, we have

$$S_{j+1} = T_{s(j+1)} H_{j+1} \quad (16)$$

According to the continuous conditions between adjacent layers, the following relationship can be obtained

$$S_j|_{z=h_j} = S_{j+1}|_{z=0} \quad (17)$$

Substituting Eqs. (15) and (16) into Equation (17) yields

$$T_{s(j+1)}|_{z=0} H_{j+1} = T_{sj}|_{z=h_j} H_j \quad (18)$$

Using left multiplication inverse matrix of $T_{s(j+1)}|_{z=0}$ by the two sides of Eq. (18), it arrives

$$H_{j+1} = T_j H_j = (T_{s(j+1)}|_{z=0})^{-1} \cdot T_{sj}|_{z=h_j} \cdot H_j \quad (19)$$

Therefore, the amplitude vector of each layer can be associated with the top layer in accordance with the recursive Eq. (19) and can be expressed as

$$H_j = T_{j1} H_1 = T_{j-1} \cdot T_{j-2} \cdots T_1 H_1 \quad (20)$$

where T_{j1} is a matrix of 6×6 .

The relationship between the amplitude vector of the bedrock and that of the bottom layer can be established based on Eq. (9).

$$(T_n|_{z=0})_{4 \times 4} (H_n)_{4 \times 1} = (T'_{s(n-1)}|_{z=h_{n-1}})_{4 \times 6} (H_{n-1})_{6 \times 1} \quad (21)$$

By defining $n-1$ equal to j in Eq. (21), the following equation can be obtained

$$(H_n)_{4 \times 1} = T_n H_1 = (T_n|_{z=0})_{4 \times 4} (T'_{s(n-1)}|_{z=h_{n-1}})_{4 \times 6} (T_{(n-1)1})_{6 \times 6} (H_1)_{6 \times 1} \quad (22)$$

There are three kinds of upward-travelling waves in saturated soils.

Each wave will produce a waveform conversion when reaching the top layer, and therefore three corresponding downward-travelling waves in the first layer can be generated.

$$F_{P11} = r_{P1P1}E_{P11} + r_{P2P1}E_{P21} + r_{SP1}E_{S1} \quad (23a)$$

$$F_{P21} = r_{P1P2}E_{P11} + r_{P2P2}E_{P21} + r_{SP2}E_{S1} \quad (23b)$$

$$F_{S1} = r_{P1S}E_{P11} + r_{P2S}E_{P21} + r_{SS}E_{S1} \quad (23c)$$

where F_{P11} , F_{P21} and F_{S1} are the potential amplitudes of the three corresponding upward-travelling waves respectively; r_{mn} is the reflection coefficient of the interface; m and n represent the incident wave and reflected wave respectively. For example, r_{P1P2} is the amplitude ratio of the reflected wave of $P2$ to incident wave of $P1$ when the incident wave is the $P1$ wave.

Substituting Eq. (23) into Eq. (13) yields

$$H_1 = (E_{P11}, r_{P1P1}E_{P11} + r_{P2P1}E_{P21} + r_{SVP1}E_{S1}, E_{P21},$$

$$r_{P1P2}E_{P11} + r_{P2P2}E_{P21} + r_{SVP2}E_{S1}, E_{S1}, r_{P1SV}E_{P11} + r_{P2SV}E_{P21} + r_{SVSV}E_{S1})^T \quad (24)$$

where H_1 is made up of upward-travelling waves (E_{P11} , E_{P21} , E_{S1}) and nine reflection coefficients.

2.4. Refraction and reflection at interfaces of saturated soil under surface water

This section investigates the wave refraction and reflection of waves at interface of saturated soil under surface water. Three different types of waves (i.e., $P1$, $P2$ and SV waves) are generated when the plane P wave travels from the bedrock to the saturated soils. These three waves continue to propagate upward in the saturated soils and will generate three corresponding downward-travelling waves at the interface between the saturated soil and the overlying water. As shown in Fig. 2, θ is the incident angle of the P wave; α_1 and α_2 are the reflection angles of the P and SV waves at the layer interface respectively; β_1 , β_2 and β_3 are the refraction angles of the $P1$, SV and $P2$ waves in saturated soils respectively. β_{c1} , β_{c2} and β_{c3} are the cumulative refraction angles of the $P1$, SV and $P2$ waves when wave propagates upwards to the top layer soil respectively. It is noted that the local coordinate system is employed in Fig. 2.

According to the Snell's law, the horizontal wave numbers of harmonic waves are the same in x -direction. When the incident angle of the P wave is θ , the following equations can be obtained.

$$k_S \sin \theta = k_P \sin \alpha = \delta_1 w_{11} = \delta_2 w_{21} = \delta_3 w_{31} \quad (25)$$

$$k_S \sin \theta = k_P \sin \alpha = \frac{\omega}{c_1} \sin \beta_1 = \frac{\omega}{c_2} \sin \beta_2 = \frac{\omega}{c_3} \sin \beta_3 \quad (26)$$

When the incident wave is the $P1$ wave at the interface between saturated soils and overlying water, $E_{P2} = 0$ and $E_{SV} = 0$, as shown in Fig.2.

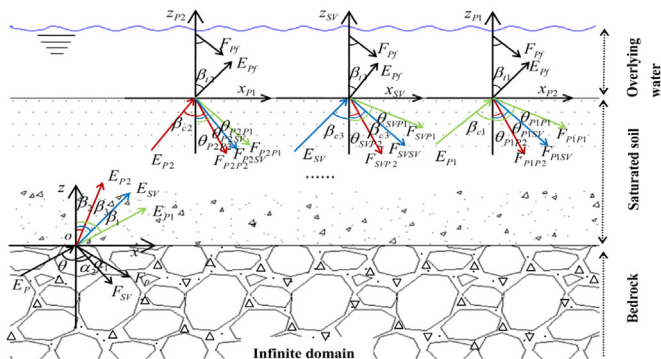


Fig. 2. The refraction and reflection of waves at the interfaces.

According to Eqs. (1) and (2), the potential functions can be expressed as

$$\phi_1 = E_{P1}e^{i[\omega t - \delta_1 w_{11}x - \delta_1 w_{13}z]} + F_{P1}e^{i[\omega t - \delta_1 w_{11}x + \delta_1 w_{13}z]}, \quad \phi_2 = F_{P2}e^{i[\omega t - \delta_2 w_{21}x + \delta_2 w_{23}z]} \quad (27a)$$

$$\psi_1 = F_S e^{i[\omega t - \delta_3 w_{31}x + \delta_3 w_{33}z]} \quad (27b)$$

Substituting Eqs. (27a) and (27b) into Eq. (10), the reflection coefficients of r_{P1P1} , r_{P1P2} and r_{P1SV} can be obtained.

Similarly, when the incident wave is the $P2$ wave, $E_{P1} = 0$ and $E_{SV} = 0$, as shown in Fig. 2.

According to Eqs. (1) and (2), the potential functions can be expressed as

$$\phi_1 = F_{P1}e^{i[\omega t - \delta_1 w_{11}x + \delta_1 w_{13}z]}, \quad \phi_2 = E_{P2}e^{i[\omega t - \delta_2 w_{21}x - \delta_2 w_{23}z]} + F_{P2}e^{i[\omega t - \delta_2 w_{21}x + \delta_2 w_{23}z]} \quad (28a)$$

$$\psi_1 = F_S e^{i[\omega t - \delta_3 w_{31}x + \delta_3 w_{33}z]} \quad (28b)$$

Substituting Eqs. (28a) and (28b) into Eq. 10, the reflection coefficients of r_{P2P1} , r_{P2P2} and r_{P2SV} can be obtained.

Similarly, when the incident wave is the SV wave, $E_{P1} = 0$ and $E_{P2} = 0$, as shown in Fig.2.

According to Eqs. (1) and (2), the potential functions can be expressed as

$$\phi_1 = F_{P1}e^{i[\omega t - \delta_1 w_{11}x + \delta_1 w_{13}z]}, \quad \phi_2 = F_{P2}e^{i[\omega t - \delta_2 w_{21}x + \delta_2 w_{23}z]} \quad (29a)$$

$$\psi_1 = E_S e^{i[\omega t - \delta_3 w_{31}x - \delta_3 w_{33}z]} + F_S e^{i[\omega t - \delta_3 w_{31}x + \delta_3 w_{33}z]} \quad (29b)$$

Substituting Eqs. (29a) and (29b) into Eq. (10), the reflection coefficients of r_{SVP1} , r_{SVP2} and r_{SVSV} can be obtained.

Substituting the nine reflection coefficients into Eq. (24), H_1 can be simplified and it contains only three unknowns (E_{P11} , E_{P21} , E_{S1}).

2.5. Derivation of transfer function in saturated soil under surface water

This section investigates the transfer functions in saturated soil under surface water. As the downward-travelling waves can be represented by the upward-travelling waves, there are three unknowns (E_{P11} , E_{P21} , E_{S1}) in H_1 and two unknowns (E_{Pn} , E_{Sn}) in H_n . However, T_{n1} is a matrix of 4×6 and four equations can be established. Therefore, it is necessary to add an equation. Assuming that the bedrock is impervious, i.e. $\phi_j(U_{ij} - u_{ij}) = 0$, then a new matrix $(T_{n1})_{5 \times 6}$ is established and the following equations can be obtained

$$E_{Pn} = a_{11}E_{P11} + a_{12}E_{P21} + a_{13}E_{S1} \quad (30a)$$

$$F_{Pn} = a_{21}E_{P11} + a_{22}E_{P21} + a_{23}E_{S1} \quad (30b)$$

$$E_{Sn} = a_{31}E_{P11} + a_{32}E_{P21} + a_{33}E_{S1} \quad (30c)$$

$$F_{Sn} = a_{41}E_{P11} + a_{42}E_{P21} + a_{43}E_{S1} \quad (30d)$$

$$0 = a_{51}E_{P11} + a_{52}E_{P21} + a_{53}E_{S1} \quad (30e)$$

where $a_{st}(s = 1, 2, 3, 4, 5 \quad t = 1, 2, 3)$ is related to H_1 and $(T_{n1})_{5 \times 6}$ and defined in Appendix C.

Combining Eqs. (30a), (30c) and (30e) yields

$$E_{P11} = c_1 E_{Pn} + c_2 E_{Sn}, \quad E_{P21} = c_3 E_{Pn} + c_4 E_{Sn}, \quad E_{S1} = c_5 E_{Pn} + c_6 E_{Sn} \quad (31a)$$

where $c_i(i = 1, 2, 3, 4, 5, 6)$ is defined in Appendix C.

When the incident wave is the P wave, $E_{Sn} = 0$. Eq. 31a can be expressed as

$$E_{P11} = c_1 E_{Pn}, \quad E_{P21} = c_3 E_{Pn}, \quad E_{S1} = c_5 E_{Pn} \quad (31b)$$

By substituting Eq. (31b) into Eq. (24), the top amplitude vector H_1 can be expressed as

$$H_1 = (d_{11}E_{Pn}, d_{21}E_{Pn}, d_{31}E_{Pn}, d_{41}E_{Pn}, d_{51}E_{Pn}, d_{61}E_{Pn})^T \quad (32)$$

where

$$d_{11} = c_1, \quad d_{21} = r_{P1P1}c_1 + r_{P2P1}c_3 + r_{SVSP1}c_5 \quad (33a)$$

$$d_{31} = c_3, \quad d_{41} = r_{P1P2}c_1 + r_{P2P2}c_3 + r_{SVSP2}c_5 \quad (33b)$$

$$d_{51} = c_5, \quad d_{61} = r_{P1SV}c_1 + r_{P2SV}c_3 + r_{SVSV}c_5 \quad (33c)$$

By substituting Eq. (32) into Eq. (20), the amplitude vector H_j can be expressed in terms of the unknowns E_{Pn} . The stress-displacement vectors of the first and each layer are obtained by taking H_j to Eq. (15).

$$S_1 = T_{S1}H_1, \quad S_j = T_{Sj}H_j = T_{j1}H_1 \quad (34)$$

The transfer function in the vertical direction from the first layer to each layer can be obtained by the ratio of the first component of S_1 to S_j in the frequency domain.

$$TF_{1j}(\omega) = \frac{a_{11}}{a_{j1}} = \frac{a_{11}/\omega^2}{a_{j1}/\omega^2} = \frac{u_{11}}{u_{j1}} \quad (35)$$

where $TF_{1j}(\omega)$ is the transfer function between the first layer and (j)th layer and does not contain E_{Sn} ; a_{11} and u_{11} are the vertical acceleration and displacement of the first layer respectively; a_{j1} and u_{j1} are vertical acceleration and displacement of the (j)th layer respectively.

3. Derivation process for multi-support underground (sub-seabed) motions in saturated soil under surface water

The power spectral density, response spectrum and coherence function are the three necessary conditions for simulating multi-support earthquake motions. In this section, according to the ground motions generated by the prototype spectral representation method [22] and the transfer functions, the underground PSD and response spectrum are first obtained and then the underground coherence function is derived accordingly. These three theoretical models are used to establish the power spectral matrix. The underground motions are generated by using the Cholesky decomposition method.

3.1. Derivation process of underground (sub-seabed) PSD and response spectrum

The difference of PSD function and response spectrum induces spatial variability, affected by the position of horizontal distance and depth. The geological strata geometry is given in Fig. 3.

The Clough-Penzien model [13] is chosen as the target ground PSD for the simulation

$$S(\omega) = \frac{\left(\omega_f^4 + 4\xi_f^2\omega_f^2\omega^2\right) \cdot S_0}{\left(\omega_g^2 - \omega^2\right) + 4\xi_g^2\omega_g^2\omega^2 \left(\omega_f^2 - \omega^2\right) + 4\xi_f^2\omega_f^2\omega^2} \cdot \omega^4 \quad (36)$$

where S_0 is the spectral intensity; ω_g and ξ_g are the ground predominant frequency and damping ratio respectively; ω_f and ξ_f are seismic energy parameters and $\omega^4/((\omega_f^2 - \omega^2) + 4\xi_f^2\omega_f^2\omega^2)$ represents a modified

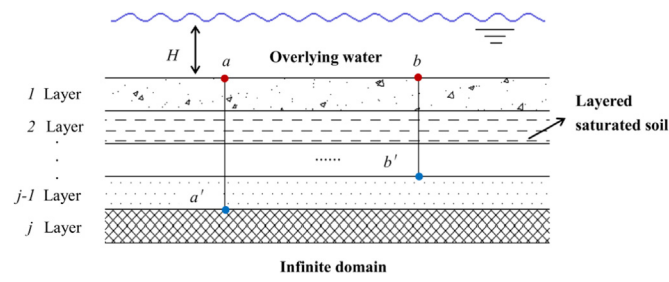


Fig. 3. Geological strata geometry containing four different points.

coefficient for the changes of seismic energy of low frequency. In this paper, the values of S_0 , ω_g , ξ_g , ω_f and ξ_f are assigned as 0.042, 21.40, 0.075, 0.38, and 0.49 respectively [25].

The underground PSD can be calculated as follow

$$S_{a'a'}(\omega) = |TF_{aa'}(\omega)|^2 \cdot S_{aa}(\omega) \quad (37)$$

where $S_{aa}(\omega)$ and are the auto-power spectrums of the motions at points a and a' in saturated soils respectively; $TF_{aa'}(\omega)$ is the transfer function between the (a)th layer and (a')th layer.

Response spectrum of Bridge Seismic Design Code (MOHURD 2011) is chosen as the target ground response spectrum. The relationship between $R_{a'}(\omega, \xi)$ and $R_a(\omega, \xi)$ can be expressed as follows

$$R_{a'}(\omega, \xi) = |TF_{aa'}(\omega)| \cdot R_a(\omega, \xi) \quad (38)$$

where ξ is a parameter related to exceeding probability, period, circular frequency and damping ratio; $R_a(\omega, \xi)$ and $R_{a'}(\omega, \xi)$ are the response spectrum of the motions at points a and a' respectively.

3.2. Derivation process of underground (sub-seabed) coherence function

The coherence function is affected by three factors, i.e. the site conditions, fluid-saturated media conditions and seismic characteristics. Therefore the formation of ground motions will be affected by these factors and the structural dynamic response is uncertain. The Hao coherence model [22] that is able to accurately describe the regional effects, is adopted as the ground target coherence function in this paper

$$\gamma_{ab}(\omega, d) = e^{-\beta_1 d} \cdot e^{-a_1(\omega) \sqrt{d} (\omega/2\pi)^2} \quad (39)$$

where $a_1(\omega) = 2\pi/\omega + b/2\pi + c$; d is the distance between different points; β_1 , a , b and c are assigned to be 1.109×10^{-4} , 3.583×10^{-2} , -1.811×10^{-5} and -1.177×10^{-4} respectively based on the 45 seismic records of SMART-1 array event [25].

Considering linear elastic response, the cross-PSD function between any two ground motions can be expressed as

$$\begin{aligned} S_{ab}(\omega) &= \frac{1}{2\pi} \int_{-\infty}^{\infty} R_{ab}(\Delta\tau_1) e^{-i\omega\Delta\tau_1} d\Delta\tau_1 \\ &= \frac{A_{(\omega)}^{(b)}}{2\pi A_{(\omega)}^{(a)}} \int_{-\infty}^{\infty} R_{aa}(\tau_a - \tau_b + \Delta\tau_2) e^{-i\omega\Delta\tau_1} d\Delta\tau_1 \\ &= \frac{A_{(\omega)}^{(b)}}{2\pi A_{(\omega)}^{(a)}} \int_{-\infty}^{\infty} R_{aa}(\tau_a - \tau_b + \Delta\tau_2) e^{-i\omega\Delta\tau_2} e^{i\omega(\tau_b - \tau_a)} d\left(\tau_a - \tau_b + \Delta\tau_2\right) \end{aligned} \quad (40)$$

where $R_{ab}(\Delta\tau)$ is the cross coherence function between the motions at points a and b ; A represents the amplitude of harmonic motions; τ_a and τ_b are constants; $\Delta\tau_2$ is the integral variable; the superscripts a and b are related to the values of the associated variables of the harmonic motions at points a and b respectively.

When the integral interval tends to be infinite, it should be noted that the final results are not affected by the initial phase difference. Eq. (40) can be expressed as

$$\begin{aligned} S_{ab}(\omega) &= \frac{A_{(\omega)}^{(b)}}{2\pi A_{(\omega)}^{(a)}} \int_{-\infty}^{\infty} R_{aa}(\Delta\tau_2) e^{-i\omega\Delta\tau_2} e^{i\omega(\tau_b - \tau_a)} d\Delta\tau_2 \\ &= \frac{A_{(\omega)}^{(b)}}{2\pi A_{(\omega)}^{(a)}} e^{i\omega(\tau_b - \tau_a)} S_{aa}(\omega) \end{aligned} \quad (41)$$

Similarly, the cross-PSD for the underground motions, $S_{a'b'}(\omega)$, can be shown

$$S_{a'b'}(\omega) = \frac{A_{(\omega)}^{(b')}}{2\pi A_{(\omega)}^{(a')}} e^{i\omega(\tau_{b'} - \tau_{a'})} S_{a'a'}(\omega) \quad (42)$$

The relation between the two coherence functions of ground and underground motions can be expressed as

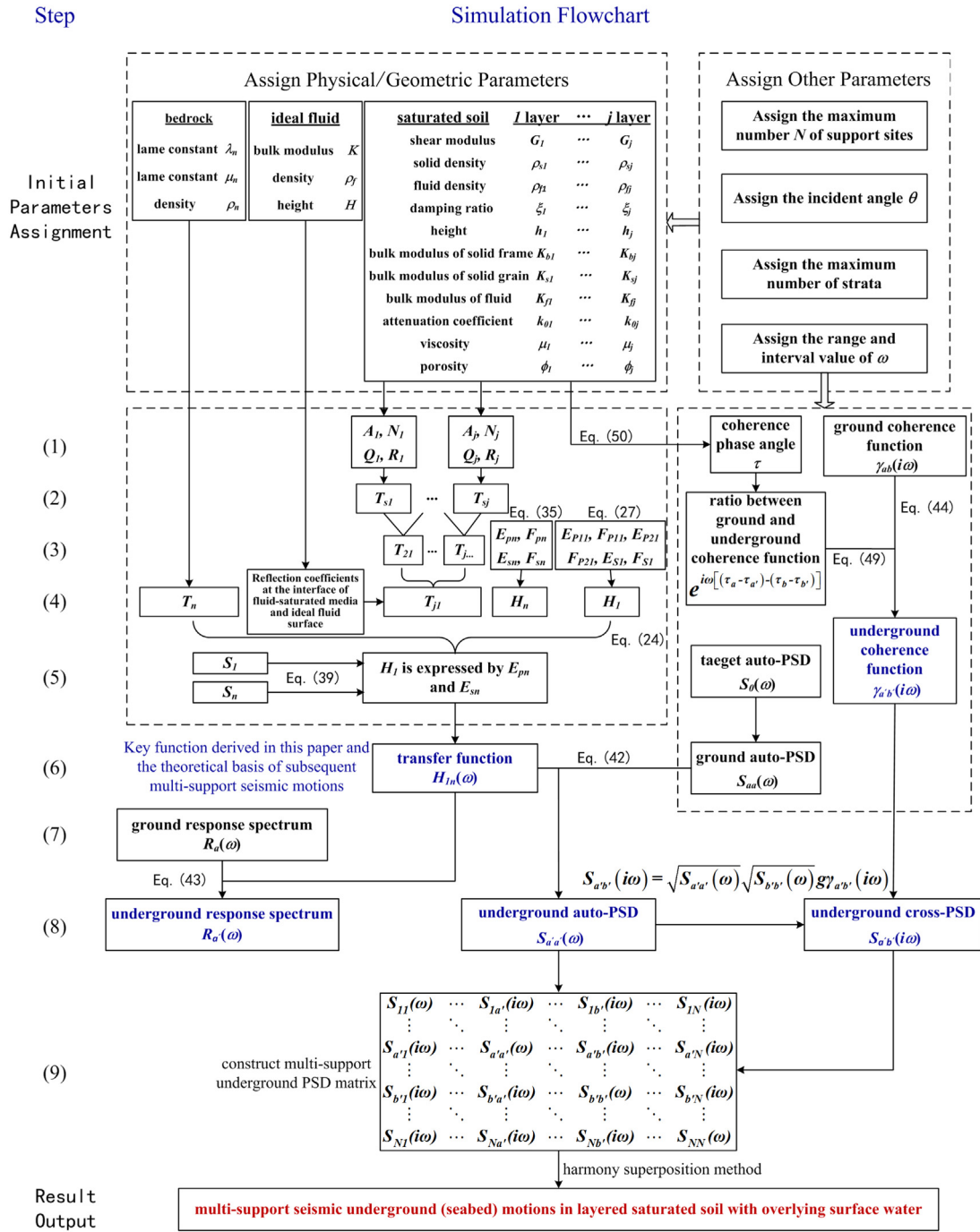


Fig. 4. Steps and flowchart for simulation.

Table 1
Material parameters for layered saturated soil.

Layer	Shear modulus G (MPa)	Solid density ρ_s (kg/m ³)	Damping ratio ξ	Bulk modulus			Attenuation coefficient k_o (m ²)	Viscosity μ (Pa s)	Porosity ϕ
				Solid frame K_b (MPa)	Solid grain K_s (MPa)	Fluid K_f (MPa)			
1	81	2550	0.05	7610	31,600	2160	1.0×10^{-10}	0.001	0.29
2	80	2560	0.05	7410	32,600	2160	1.0×10^{-10}	0.001	0.30
3	79	2650	0.05	7210	33,600	2160	1.0×10^{-10}	0.001	0.305
4	78	2700	0.05	7010	34,600	2160	1.0×10^{-10}	0.001	0.32

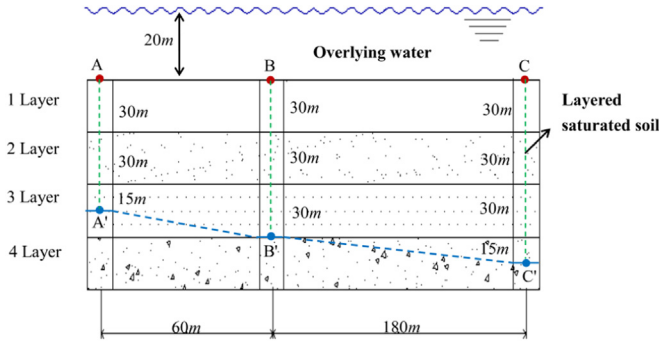


Fig. 5. Layered saturated soil for the case study.

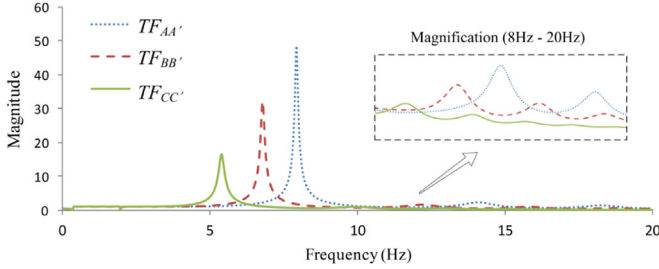


Fig. 6. Comparison of transfer functions at three monitoring points of different layer thickness (15").

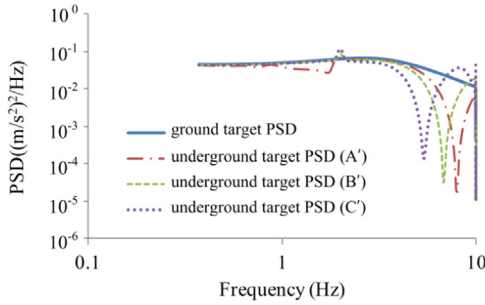


Fig. 7. Comparison between ground and underground target PSD (15").

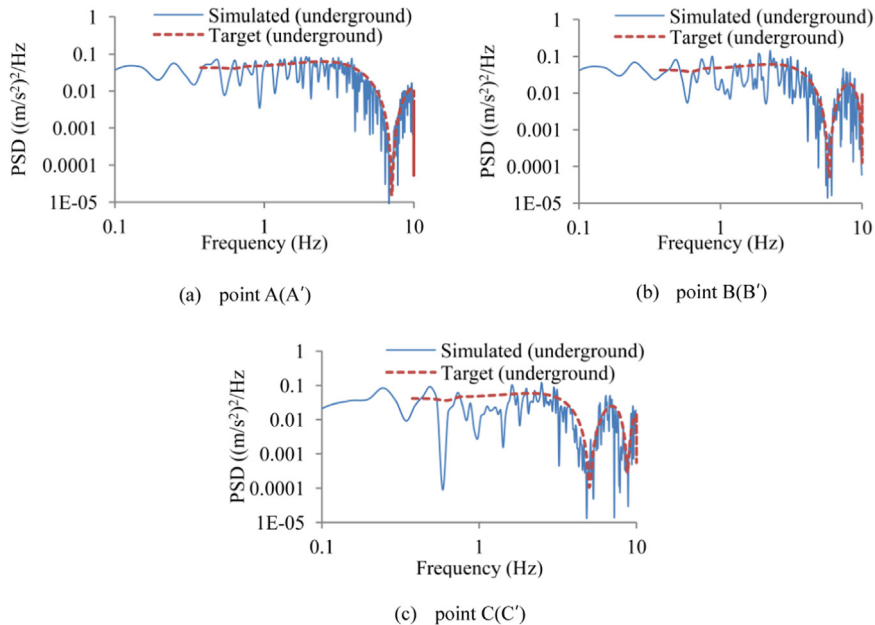


Fig. 8. Comparison between underground target and simulated PSD (15").

$$\frac{\gamma_{a'b'}(\omega)}{\gamma_{ab}(\omega)} = \frac{S_{a'b'}(\omega) \cdot \sqrt{S_{aa}(\omega) S_{bb}(\omega)}}{S_{ab}(\omega) \cdot \sqrt{S_{a'a'}(\omega) S_{b'b'}(\omega)}} = \frac{S_{a'b'}(\omega)}{S_{ab}(\omega)} \cdot |TF_{aa'}(\omega)| \cdot |TF_{bb'}(\omega)| \quad (43)$$

where $\gamma_{ab}(\omega)$ and $\gamma_{a'b'}(\omega)$ are coherence functions for ground and underground motions respectively.

Substituting Eqs. (37), (41) and (42) into Eq. 43, underground coherence functions can be expressed as [29]

$$\gamma_{a'b'}(\omega) = \gamma_{ab}(\omega) \cdot e^{i\omega(\tau_a - \tau_{a'})} e^{i\omega(\tau_b - \tau_{b'})} = \gamma_{ab}(\omega) \cdot e^{i\omega[(\tau_a - \tau_{a'}) - (\tau_b - \tau_{b'})]} \quad (44)$$

The values of τ_a , τ_b , $\tau_{a'}$ and $\tau_{b'}$ can be calculated from the following equation

$$\tau = \frac{k^* z}{\omega} = \sqrt{\frac{\rho}{G^*}} z \quad (45)$$

where k^* and G^* are the complex wave number and complex shear modulus respectively, and they satisfy $(k^*)^2 = \rho\omega^2 / (G + i\omega\eta) = \rho\omega^2 / G^*$, $G^* = G + i\omega\eta$, $\omega\eta = 2G\xi$ and $G^* = G(1 + 2i\xi)$; the phase angle τ varies with the ordinate value z .

4. Simulation of multi-point seismic motions in saturated soil under surface water

4.1. Implementation

A flowchart for simulating the multi-support seismic motions in saturated soil with overlying surface is first described in Fig. 4. The flowchart shows the simulation process. First, the initial parameters of bedrock, ideal fluid and saturated soil, and some other parameters such as geometry and frequency are assigned. According to the parameters, the transfer functions are firstly deduced. The ground surface PSD model is adopted by the Clough-Penzien model, and the underground PSD can be obtained by the ground surface PSD functions and the transfer functions. The Hao coherence model is adopted as the ground surface coherence function, and the underground coherence function can be obtained. Finally, the underground motions can be simulated by the obtained underground PSD functions and coherence functions.

4.2. Initial parameters

Based on the derived method of generating multi-support seismic

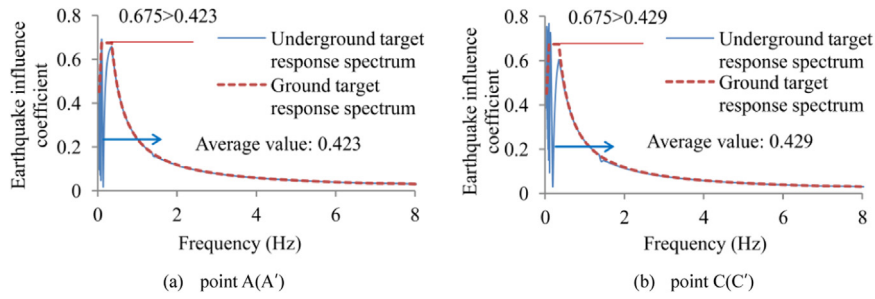


Fig. 9. Comparison between underground and ground target response spectrum (15°).

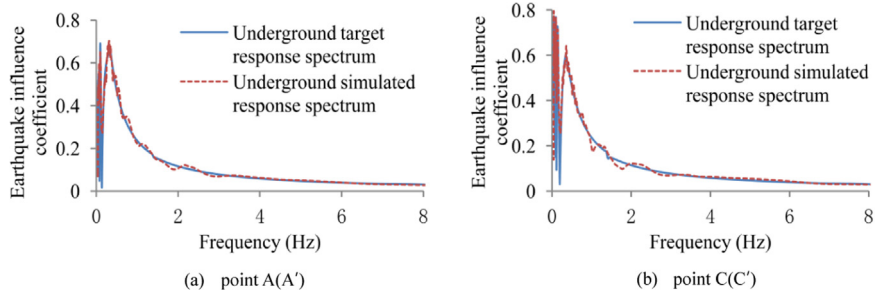


Fig. 10. Comparison between underground target and simulated response spectrum (15°).

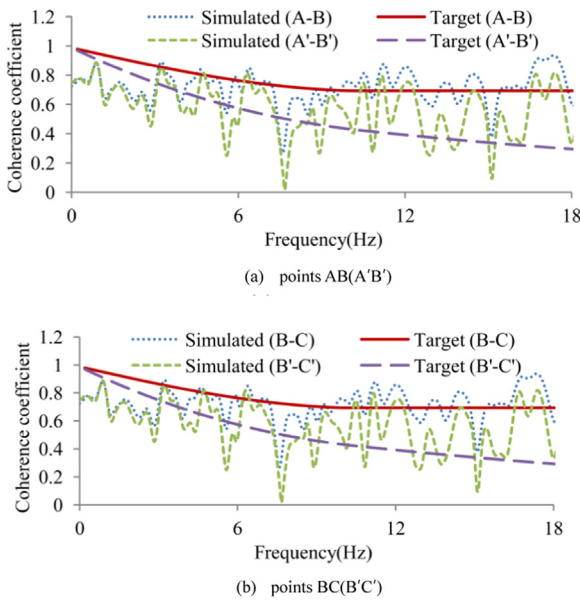


Fig. 11. Comparison between target and simulated coherence functions (15°).

underground motions in saturated soils, a program is coded and developed. It is noted that the parameters related to the PSD model, apparent wave velocity, coherence function, response spectrum, intensity envelope function, coordinates of support points and geological parameters should be given in advance. The PSD model, response spectrum and coherence function have been given in Section 3. According to the report of the geological exploration in Tianjin [36], the exploration data of the site soil geometric and material properties are listed in Table 1 and the apparent wave velocity is 250 m/s. The parameters of the bedrock are defined as $\rho_n = 3000\text{Kg/m}^3$, $\mu_n = 3.0 \times 10^9\text{Pa}$ and $\lambda_n = 2.2 \times 10^9\text{Pa}$. The parameters of the overlying water are defined as $\rho_f = 1000\text{Kg/m}^3$ and $K = 2160 \times 10^9\text{Pa}$.

4.3. Effect of soil thickness

Fig. 5 schematically shows a layered saturated soil overlain by surface water. To investigate the impact of soil thickness on the predicted underground motions, the transfer functions at three monitoring points of different soil thickness (i.e. thickness AA', BB' and CC'; incident angle is 15°) are compared in Fig. 6. In particular, Fig. 6 indicates that the dominant frequency of transfer functions decreases as the soil thickness increases.

Furthermore in Fig. 7, it can be seen that the predicted underground PSD curves are fluctuant, which shows a great difference compared to ground PSD curves. The reason for this phenomenon is that the underground PSD is determined by the ground PSD and the corresponding transfer function ($TF_{aa'}(\omega)$). The transfer function is fluctuant and dependent on specific soil properties, as shown in Fig. 6. In Fig. 8, the simulated underground PSD matches with the target underground PSD in saturated soils, which demonstrates the reliability of the derived theoretical method.

Fig. 9 compares the underground and ground target response spectrum at different points. It is noted that the underground target response spectrum fluctuates vigorously, as explained before. Moreover, it can be seen in Fig. 9 that the average value of underground target response spectrum is smaller than the plateau value of the ground target response spectrum over the period range from 0.10147 to 0.34712 s, which indicates the amplification effects by the layered saturated soil. In addition, Fig. 10 shows that the underground simulated response spectrum is consistent with the target response spectrum, which further demonstrates the reliability of the theoretical method to simulate the multi-support seismic underground motions in saturated soils with overlying water.

As shown in Fig. 11, the correlation coefficients of ground and underground are similar when the frequency is lower than 3 Hz but are significantly different when the frequency is beyond this range, consistent with Eq. (44). Comparing Fig. 11 (a) with Fig. 11 (b), it can be seen that the coherence coefficient of BC(B'C') is slightly smaller than that of AB(A'B'), which reflects the effect of horizontal distance on the coherence function. Moreover, the coherence coefficient of underground motions in saturated soil is smaller than that of ground motions, which reflects the effect of soil conditions on amplification coefficient.

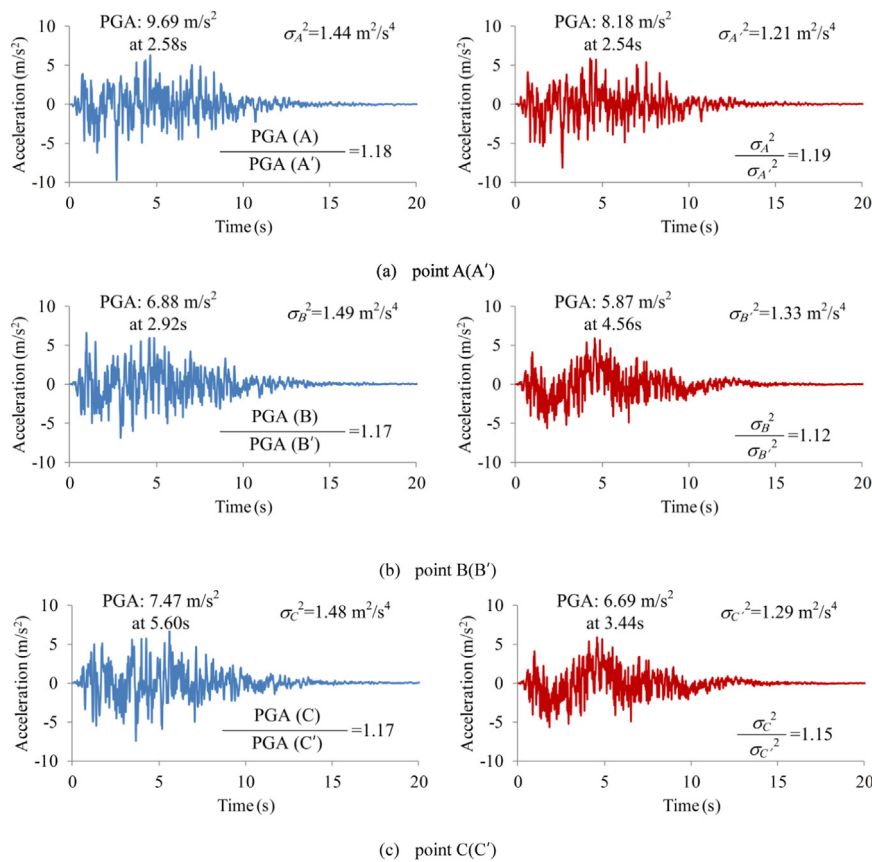


Fig. 12. Comparison of ground and underground acceleration at different points AA', BB' and CC' (15°).

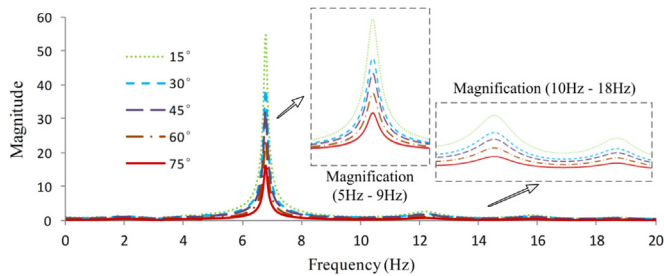


Fig. 13. Transfer functions of site soil (points AA') at different incident angles.

As we can see from Fig. 12, generally the peak values and variances of underground motions are smaller than those of ground motions. The site amplification factors of earthquake motions will become larger with the increasing layer thickness. This is consistent with the aforementioned site amplification effect.

4.4. Effect of incident angle

In this section, the effects of the incident angle on the derived transfer function in the previous section and simulated seismic motions are investigated and the regularity is summarized. The incident angles of *P* waves range from 0° to 90°, and there are two special cases below to be clarified firstly:

(a) For the case of vertical wave incidence (incident angle is 0°), the incident *P* waves cross the layer-interface vertically without horizontal component. Meanwhile, the derivative *SV* waves in the saturated soil do not exist for case of vertical wave-incidence, which is different from that for oblique incidence case.

(b) For the case of horizontal wave incidence (incident angle is 90°), the incident *P*

waves propagate horizontally and they will not cross the layer-interface in theory.

According to the analysis above, the cases for incident angles (15°, 30°, 45°, 60° and 75°) are conducted. The overlying water depth is also set to 20 m and depicted in Fig. 5. The transfer coefficients between points A and A' under different incident angles are analyzed and given in Fig. 13. It can be seen that the amplitude values of transfer functions decrease with the increasing incident angle. The reason for this phenomenon is that the total reflection components (reflection energy or downward-travelling wave energy) at the soil interface increase with increasing incidence angle, and reduces the upward-travelling wave energy (total energy conservation) and further induces the decrease of amplitude value of the transfer function.

To investigate the effect of the incident angle on the simulated seismic motions, the acceleration histories of ground and underground motions and variance ratios are given in Fig. 14. In order to illustrate more clearly, the variance ratios and incidence angles are individually given in the Fig. 15. The figures show that variance ratios get smaller with the increasing incident angle. The phenomenon is consistent with that (amplitude values of transfer functions decrease with the increasing incident angle) discussed above. Actually, in theory, amplitudes of transfer function decrease logically result in the ratios between ground and underground seismic motions, because the essence of transfer function is the proportion between ground and underground motions in frequency domain.

4.5. Effect of overlying water depth

This section discusses the effect of overlying water depth on seismic

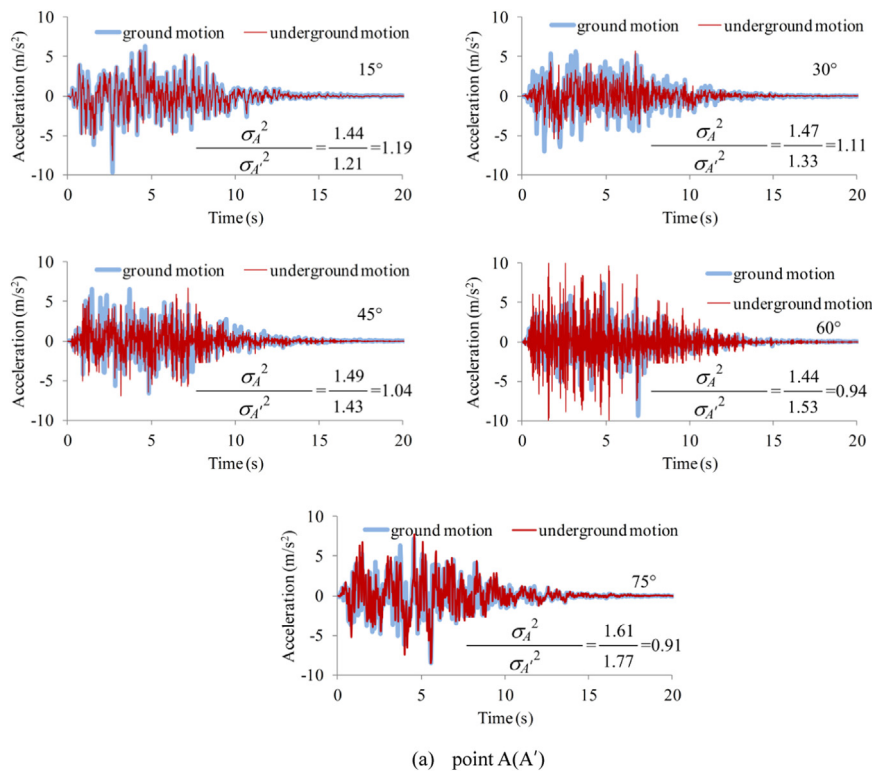


Fig. 14. Comparison of simulated ground and underground motions at different incident angles. (a) point A(A'); (b) point B(B'); and (c) point C(C').

motions. Firstly, the transfer functions of saturated soil, whose physical meaning is the ratio of ground (soil-water interface) and underground motions in frequency domain, are analyzed and illustrated for the case of different water depths (0.01 m, 1 m, 5 m, 10 m, 20 m and 50 m) in Fig. 16. The incident angle is set to 15°. It can be seen that the

amplitude of transfer function decreases with the increasing of water depth. The reason is that when the seismic waves (including *P* waves and *SV* waves) reach the interface between saturated soil and overlying water, part of *P*-wave energy will propagate into the overlying water. Specifically, comparing with the case without overlying water, *P*-

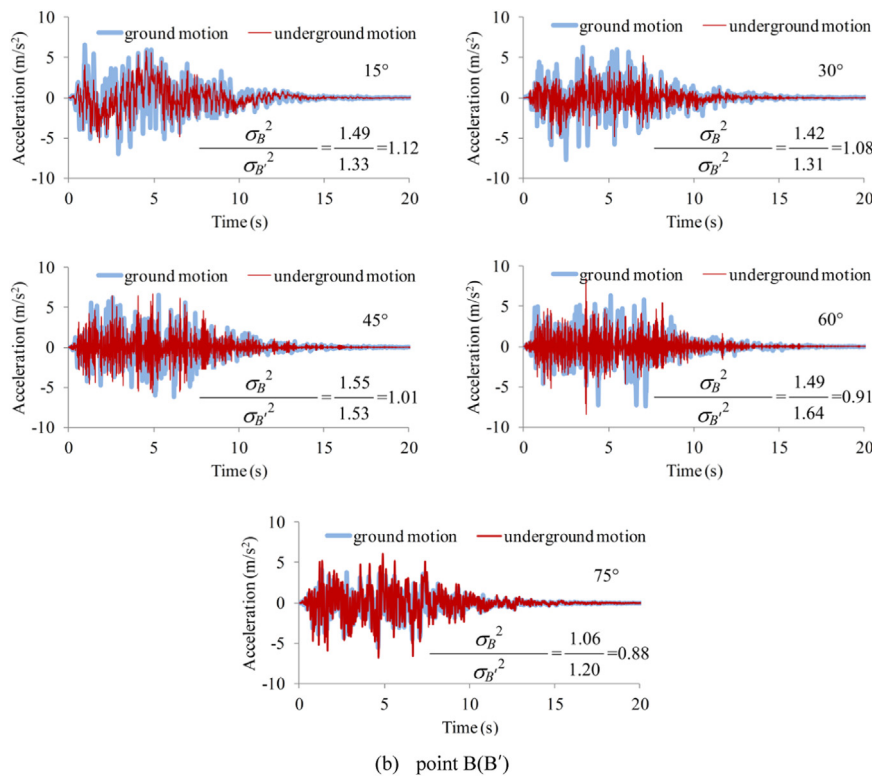
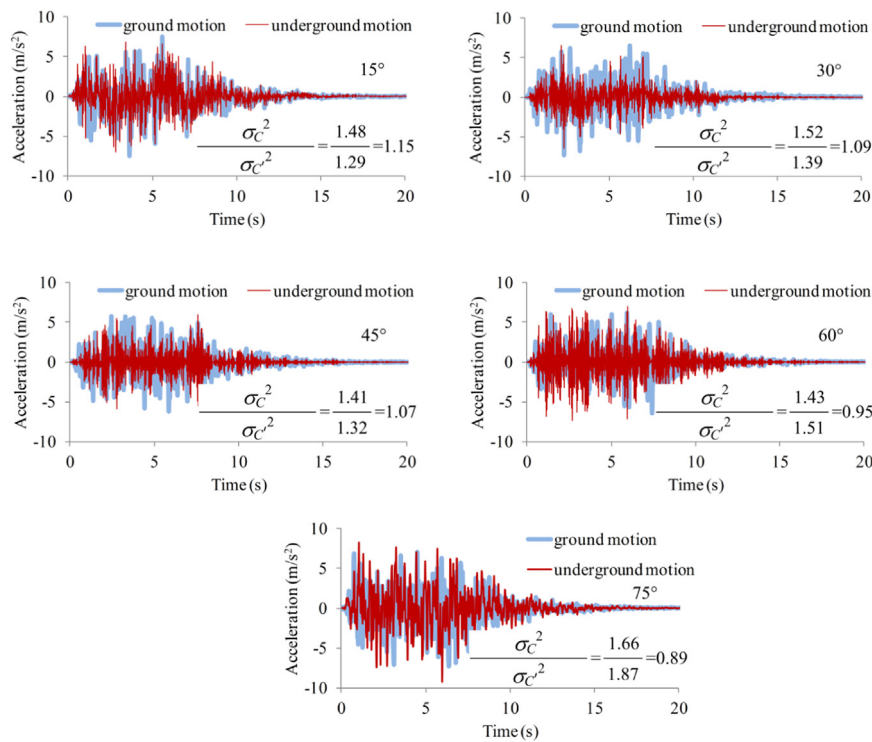


Fig. 14. (continued)



(c) point C(C')

Fig. 14. (continued)

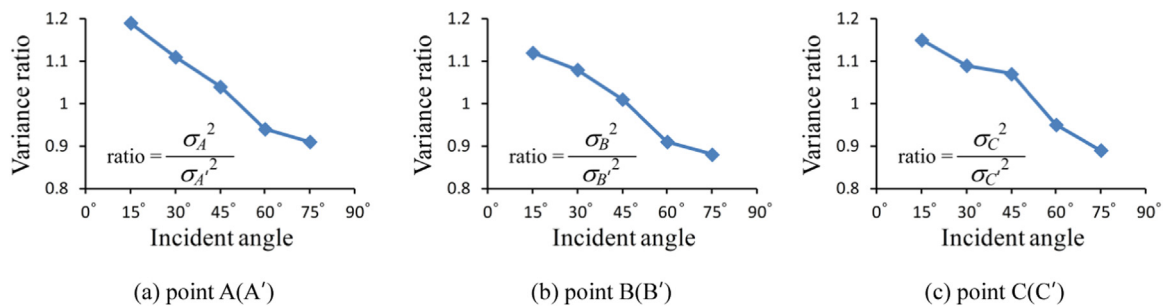


Fig. 15. Variance ratio of ground and underground motions at different incident angles. (a) point A(A'); (b) point B(B'); and (c) point C(C').

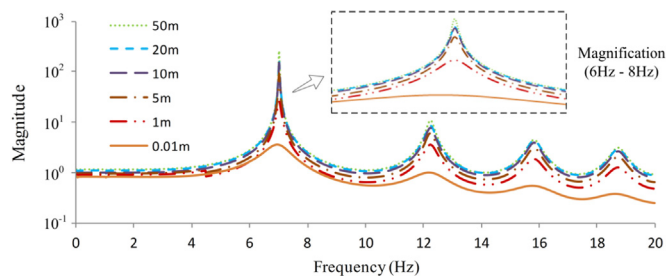


Fig. 16. Transfer functions of site soil (points AA') by different overlying water depths. Note: The case of 0.01 m-depth can be approximately regarded as the case without overlying water.

waves at soil-water interface propagate into the overlying water and cause that the energy of seismic ground motion (at soil-water interface) decreases. Meanwhile, *P*-waves energy propagation increases with the increasing of water-depth and induces that the energy of seismic ground motion decreases. So, the ratio of ground (soil-water interface) and underground motions (i.e. the amplitude of transfer function) will decrease with the increasing of water-depth.

To further clarify the effect of overlying water depths, the acceleration histories of ground and underground motions and variance ratios are given in Fig. 17. In order to illustrate more clearly, the variance ratios along with water-depth are individually given in the Fig. 18. The figures show that variance ratios get greater with the increasing overlying water depth. In essence, the phenomenon is consistent with that discussed above (i.e. amplitude values of transfer functions increase with the increasing overlying water depth).

5. Concluding remarks

This paper focuses on the investigation for predicting multi-support seismic underground (sub-seabed) motions in the layered saturated soil overlain by surface water for oblique incident *P* waves. This aims at providing a feasible approach for simulating the multi-support seismic underground motions required for the seismic analysis of large-span structures (e.g. cross-sea bridges and sub-seabed tunnels) located at the layered saturated soil with overlying surface water. The main works are summarized as follows:

- (1) The transfer functions of the layered saturated soil with overlying surface water are derived and obtained. The obtained transfer

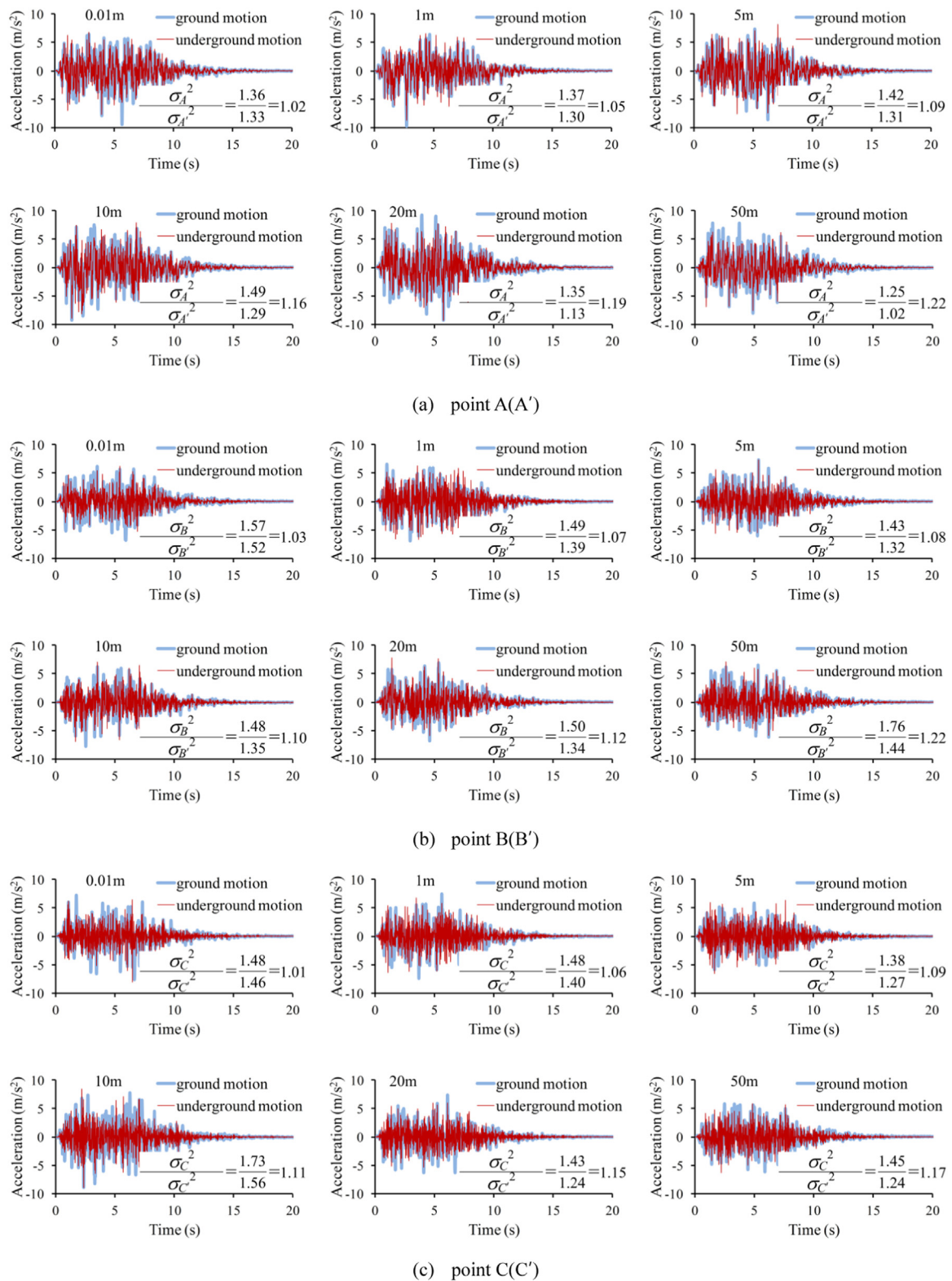


Fig. 17. Comparison of simulated ground and underground motions by different overlying water depths (0.01 m, 1 m, 5 m, 10 m, 20 m and 50 m).

function is the key theoretical basis of the subsequent numerical simulation of multi-support seismic underground motions.

- (2) The underground PSD function and underground response spectrum function are further deduced by employing the derived transfer function. Based on the two derived underground theoretical models and the additional cross-coherence function, the cross-PSD matrix is constructed and the multi-support seismic

underground motions are further generated. Meanwhile, the simulated results are validated against the target PSD, target response spectrum and target cross-coherence function.

- (3) The effects of soil thickness, incident angle and overlying water depth on the simulated seismic motions are investigated, and results show that the ratio of ground (soil-water interface) and underground motions (i.e. the amplitude of transfer function) has a

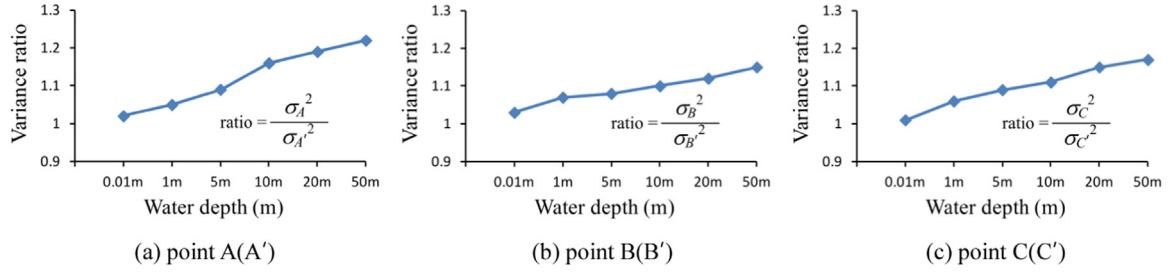


Fig. 18. Variance ratio of ground and underground motions by different overlying water depths (0.01 m, 1 m, 5 m, 10 m, 20 m and 50 m).

decreasing tendency with the soil thickness or incident angle increasing, but it increases with the overlying water depth increasing.

It should be noted that this paper focuses on the study of the multi-support seismic motions, and the earthquake-induced wave excitations are not included due to the present concentration of wave propagation investigations in geotechnical media. The relevant work will be considered in future research.

Appendix A

The parameters in T_n

$$t_{n11} = ik_{3Pn}e^{ik_{3Pn}z}, \quad t_{n12} = -ik_{3Pn}e^{-ik_{3Pn}z}, \quad t_{n13} = ik_1e^{ik_{3Pn}z}, \quad t_{n14} = ik_1e^{-ik_{3Pn}z} \quad (A1)$$

$$t_{n21} = -ik_1e^{ik_{3Pn}z}, \quad t_{n22} = -ik_1e^{-ik_{3Pn}z}, \quad t_{n23} = ik_{3Sn}e^{ik_{3Sn}z}, \quad t_{n24} = -ik_{3Pn}e^{-ik_{3Pn}z} \quad (A2)$$

$$t_{n31} = \mu_n k_{22}e^{ik_{3Pn}z}, \quad t_{n32} = \mu_n k_{22}e^{-ik_{3Pn}z}, \quad t_{n33} = -2\mu_n k_1 k_{3Sn}e^{ik_{3Sn}z}, \quad t_{n34} = 2\mu_n k_1 k_{3Sn}e^{-ik_{3Sn}z} \quad (A3)$$

$$t_{n41} = 2\mu_n k_1 k_{3Pn}e^{ik_{3Pn}z}, \quad t_{n42} = -2\mu_n k_1 k_{3Pn}e^{-ik_{3Pn}z}, \quad t_{n43} = \mu_n k_{33}e^{ik_{3Sn}z}, \quad t_{n44} = \mu_n k_{33}e^{-ik_{3Sn}z} \quad (A4)$$

where $k_{22} = -(k_1^2 + k_{3Pn}^2)(c_{Pn}^2/c_{Sn}^2) + 2k_1^2$, $k_{33} = k_1^2 - k_{3Sn}^2$

Appendix B

The parameters in T_{sj}

In the (j)th layer, each parameter of T_{sj} can be expressed as

$$t_{sj11} = i\delta_1 w_{13} e^{i\delta_1 w_{13} z}, \quad t_{sj12} = -i\delta_1 w_{13} e^{-i\delta_1 w_{13} z}, \quad t_{sj13} = i\delta_2 w_{23} e^{i\delta_2 w_{23} z} \quad (B1)$$

$$t_{sj14} = -i\delta_2 w_{23} e^{-i\delta_2 w_{23} z}, \quad t_{sj15} = i\delta_3 w_{33} e^{i\delta_3 w_{33} z}, \quad t_{sj16} = i\delta_3 w_{33} e^{-i\delta_3 w_{33} z} \quad (B2)$$

$$t_{sj21} = -i\delta_1 w_{11} e^{i\delta_1 w_{11} z}, \quad t_{sj22} = -i\delta_1 w_{11} e^{-i\delta_1 w_{11} z}, \quad t_{sj23} = -i\delta_2 w_{21} e^{i\delta_2 w_{21} z} \quad (B3)$$

$$t_{sj24} = -i\delta_2 w_{21} e^{-i\delta_2 w_{21} z}, \quad t_{sj25} = i\delta_3 w_{33} e^{i\delta_3 w_{33} z}, \quad t_{sj26} = -i\delta_3 w_{33} e^{-i\delta_3 w_{33} z} \quad (B4)$$

$$t_{sj31} = -[A + (R + Q)\beta_1 + Q + 2Nw_{13}^2]\delta_1^2 e^{i\delta_1 w_{13} z} \quad (B5)$$

$$t_{sj32} = -[A + (R + Q)\beta_1 + Q + 2Nw_{13}^2]\delta_1^2 e^{-i\delta_1 w_{13} z} \quad (B6)$$

$$t_{sj33} = -[A + (R + Q)\beta_2 + Q + 2Nw_{23}^2]\delta_2^2 e^{i\delta_2 w_{23} z} \quad (B7)$$

$$t_{sj34} = -[A + (R + Q)\beta_2 + Q + 2Nw_{23}^2]\delta_2^2 e^{-i\delta_2 w_{23} z} \quad (B8)$$

$$t_{sj35} = -2N\delta_3^2 w_{31} w_{33} e^{i\delta_3 w_{33} z}, \quad t_{sj36} = 2N\delta_3^2 w_{31} w_{33} e^{-i\delta_3 w_{33} z} \quad (B9)$$

$$t_{sj41} = 2N\delta_1^2 w_{11} w_{13} e^{i\delta_1 w_{13} z}, \quad t_{sj42} = -2N\delta_1^2 w_{11} w_{13} e^{-i\delta_1 w_{13} z}, \quad t_{sj43} = 2N\delta_2^2 w_{21} w_{23} e^{i\delta_2 w_{23} z} \quad (B10)$$

$$t_{sj44} = -2N\delta_2^2 w_{21} w_{23} e^{-i\delta_2 w_{23} z}, \quad t_{sj45} = -N\delta_3^2 (w_{33}^2 - w_{31}^2) e^{i\delta_3 w_{33} z}, \quad t_{sj46} = -N\delta_3^2 (w_{33}^2 - w_{31}^2) e^{-i\delta_3 w_{33} z} \quad (B11)$$

$$t_{sj51} = (Q + R\beta_1)/\phi \cdot \delta_1^2 e^{i\delta_1 w_{13} z}, \quad t_{sj52} = (Q + R\beta_1)/\phi \cdot \delta_1^2 e^{-i\delta_1 w_{13} z}, \quad t_{sj53} = (Q + R\beta_2)/\phi \cdot \delta_2^2 e^{i\delta_2 w_{23} z} \quad (B12)$$

$$t_{sj54} = (Q + R\beta_2)/\phi \cdot \delta_2^2 e^{-i\delta_2 w_{23} z}, \quad t_{sj55} = 0, \quad t_{sj56} = 0 \quad (B13)$$

$$t_{sj61} = i\phi(\beta_1 - 1)\delta_1 w_{13} e^{i\delta_1 w_{13} z}, \quad t_{sj62} = -i\phi(\beta_1 - 1)\delta_1 w_{13} e^{-i\delta_1 w_{13} z}, \quad t_{sj63} = i\phi(\beta_2 - 1)\delta_2 w_{23} e^{i\delta_2 w_{23} z} \quad (B14)$$

$$t_{sj64} = -i\phi(\beta_2 - 1)\delta_2 w_{23} e^{-i\delta_2 w_{23} z}, \quad t_{sj65} = i\phi(\alpha_0 - 1)\delta_3 w_{31} e^{i\delta_3 w_{33} z}, \quad t_{sj66} = i\phi(\alpha_0 - 1)\delta_3 w_{31} e^{-i\delta_3 w_{33} z} \quad (B15)$$

Appendix C

The parameters involved in Eqs. (42) and (43).

$$a_{11} = t_{n11} + t_{n12}r_{p1p1} + t_{n14}r_{p1p2} + t_{n16}r_{p1s} \quad (C1)$$

$$a_{12} = t_{n12}r_{p2p1} + t_{n13} + t_{n14}r_{p2p2} + t_{n16}r_{p2s} \quad (C2)$$

$$a_{13} = t_{n12}r_{sp1} + t_{n14}r_{sp2} + t_{n15} + t_{n16}r_{ss} \quad (C3)$$

$$a_{31} = t_{n31} + t_{n32}r_{p1p1} + t_{n34}r_{p1p2} + t_{n36}r_{p1s} \quad (C4)$$

$$a_{32} = t_{n32}r_{p2p1} + t_{n33} + t_{n34}r_{p2p2} + t_{n36}r_{p2s} \quad (C5)$$

$$a_{33} = t_{n32}r_{sp1} + t_{n34}r_{sp2} + t_{n35} + t_{n36}r_{ss} \quad (C6)$$

$$a_{51} = t_{n51} + t_{n52}r_{p1p1} + t_{n54}r_{p1p2} + t_{n56}r_{p1s} \quad (C7)$$

$$a_{52} = t_{n52}r_{p2p1} + t_{n53} + t_{n54}r_{p2p2} + t_{n56}r_{p2s} \quad (C8)$$

$$a_{53} = t_{n52}r_{sp1} + t_{n54}r_{sp2} + t_{n55} + t_{n56}r_{ss} \quad (C9)$$

$$c_1 = \frac{-a_{53} \cdot (a_{53} \cdot a_{32} - a_{33} \cdot a_{52})}{(a_{53} \cdot a_{31} - a_{33} \cdot a_{51}) \cdot (a_{53} \cdot a_{12} - a_{13} \cdot a_{52}) - (a_{53} \cdot a_{11} - a_{13} \cdot a_{51}) \cdot (a_{53} \cdot a_{32} - a_{33} \cdot a_{52})} \quad (C10)$$

$$c_2 = \frac{a_{53} \cdot (a_{53} \cdot a_{12} - a_{13} \cdot a_{52})}{(a_{53} \cdot a_{31} - a_{33} \cdot a_{51}) \cdot (a_{53} \cdot a_{12} - a_{13} \cdot a_{52}) - (a_{53} \cdot a_{11} - a_{13} \cdot a_{51}) \cdot (a_{53} \cdot a_{32} - a_{33} \cdot a_{52})} \quad (C11)$$

$$c_3 = \frac{a_{53} \cdot (a_{53} \cdot a_{31} - a_{33} \cdot a_{51})}{(a_{53} \cdot a_{31} - a_{33} \cdot a_{51}) \cdot (a_{53} \cdot a_{12} - a_{13} \cdot a_{52}) - (a_{53} \cdot a_{11} - a_{13} \cdot a_{51}) \cdot (a_{53} \cdot a_{32} - a_{33} \cdot a_{52})} \quad (C12)$$

$$c_4 = \frac{-a_{53} \cdot (a_{53} \cdot a_{11} - a_{13} \cdot a_{51})}{(a_{53} \cdot a_{31} - a_{33} \cdot a_{51}) \cdot (a_{53} \cdot a_{12} - a_{13} \cdot a_{52}) - (a_{53} \cdot a_{11} - a_{13} \cdot a_{51}) \cdot (a_{53} \cdot a_{32} - a_{33} \cdot a_{52})} \quad (C13)$$

$$c_5 = \frac{a_{51} \cdot (a_{53} \cdot a_{32} - a_{33} \cdot a_{52}) - a_{52} \cdot (a_{53} \cdot a_{31} - a_{33} \cdot a_{51})}{(a_{53} \cdot a_{31} - a_{33} \cdot a_{51}) \cdot (a_{53} \cdot a_{12} - a_{13} \cdot a_{52}) - (a_{53} \cdot a_{11} - a_{13} \cdot a_{51}) \cdot (a_{53} \cdot a_{32} - a_{33} \cdot a_{52})} \quad (C14)$$

$$c_6 = \frac{-(a_{51} \cdot (a_{53} \cdot a_{12} - a_{13} \cdot a_{52}) - a_{52} \cdot (a_{53} \cdot a_{11} - a_{13} \cdot a_{51}))}{(a_{53} \cdot a_{31} - a_{33} \cdot a_{51}) \cdot (a_{53} \cdot a_{12} - a_{13} \cdot a_{52}) - (a_{53} \cdot a_{11} - a_{13} \cdot a_{51}) \cdot (a_{53} \cdot a_{32} - a_{33} \cdot a_{52})} \quad (C15)$$

where t_{nij} is a parameter of i th rows and j th columns of $(T_{n1})_{5 \times 6}$.

References

- Alexander NA. Multi-support excitation of single span bridges, using real seismic ground motion recorded at the SMART-1 array. *Comput Struct* 2008;86(1–2):88–103.
- Bao Z, Yuan Y, Yu HT. Multi-scale physical model of shield tunnels applied in shaking table test. *Soil Dyn Earthq Eng* 2017;100:465–79.
- Berrah M, Kausel E. Response spectrum analysis of structures subjected to spatially varying motion. *Earthq Eng Struct Dyn* 1992;21(6):461–70.
- Bi KM, Hao H. Influence of irregular topography and random soil properties on coherency loss of spatial seismic ground motions. *Earthq Eng Struct Dyn* 2011;40(9):1045–61.
- Bi KM, Hao H. Modelling and simulation of spatially varying earthquake ground motions at sites with varying conditions. *Probabilistic Eng Mech* 2012;29:92–104.
- Biot MA. Theory of propagation of elastic waves in a fluid-saturated porous solid. *J Acoust Soc Am* 1956;28(2):168–91.
- Biot MA, Willis DG. The elastic coefficients of the theory of consolidation. *J Appl Mech* 1957;15(2):594–601.
- Biot MA. Mechanics of deformation and acoustic propagation in porous media. *J Appl Phys* 1962;33(4):1482–98.
- Boore DM. Analysis of earthquake recordings obtained from the Seafloor Earthquake Measurement System (SEMS) instruments deployed off the coast of southern California. Open-File Report 97-733, US Geological Survey; 1997.
- Boore DM, Smith CE. Analysis of earthquake recordings obtained from the Seafloor Earthquake measurement system (SEMS) instruments deployed off the coast of southern California. *Bull Seismol Soc Am* 1999;89(1):260–74.
- Brekhovskikh LM. *Waves in layered media*. 2nd ed New York: Academic Press; 1980.
- Chen B, Wang D, Li H, Sun Z, Shi Y. Characteristics of earthquake ground motion on the seafloor. *J Earthq Eng* 2015;19(6):874–904.
- Clough RW, Penzien J. *Dynamics of structures*. 2nd ed New York: McGraw-Hill, Inc; 1993.
- Davoodi M, Jafari MK, Sadroldini SMA. Effect of multi-support excitation on seismic response of embankment dams. *Int J Civil Eng* 2013;11(1B):19–28.
- Deodatis G. Non-stationary stochastic vector processes: seismic ground motion applications. *Probabilistic Eng Mech* 1996;11(3):149–67.
- Deodatis G, Arwade S, Shinozuka M. Seismic response of bridges to differential support ground motion. *Natl Cent Earthq Eng Res* 1997;97-0005:223–36.
- Dorman J. Period equation for waves of Rayleigh type on a layered, liquid-solid half space. *Bull Seismol Soc Am* 1962;52(2):389–97.
- Ewing WM, Jardetzky WS, Press F. *Elastic waves in layered media*. New York: McGraw-Hill; 1957.
- Guo W, Yu ZW, Liu GH, Guo Z. Possible existing seismic analysis errors of long span structures and bridges while utilizing multi-point earthquake calculation models. *Bull Earthq Eng* 2013;11(5):1683–710.
- Ha SJ, Han SW. An efficient method for selecting and scaling ground motions matching target response spectrum mean and variance. *Earthq Eng Struct Dyn* 2016;45(8):1381–7.
- Hao H. Effects of spatial variation of ground motion on large multiply-supported structures. in: EERC Rep No89-06, Earthquake Engineering Research Center, University of California, Berkeley; 1989.
- Hao H, Oliveira CS, Penzien J. Multiple-station ground motion processing and simulation based on smart-1 array data. *Nucl Eng Des* 1989;111(3):293–310.
- Harichandran RS, Vanmarcke EH. Stochastic variation of earthquake ground motion in space and time. *J Eng Mech* 1986;112(2):154–74.
- Hu L, Xu YL, Zheng Y. Conditional simulation of spatially variable seismic ground motions based on evolutionary spectra. *Earthq Eng Struct Dyn* 2012;41(15):2125–39.
- Kaul MK. Stochastic characterization of earthquakes through their response spectrum. *Earthq Eng Struct Dyn* 1978;6(5):497–509.
- Konakli K, Kiureghian AD. Simulation of spatially varying ground motions including incoherence, wave-passage and differential site-response effects. *Earthq Eng Struct Dyn* 2012;41(3):495–513.
- Liang S, Shi LD, Kato S. A new average response spectrum method for linear response analysis of structures to spatial earthquake ground motion. *Eng Struct* 2006;28(13):1835–42.
- Liu GH, Lu XZ, Guo W. Multi-point seismic motions based on focal mechanism and considering local site multi-layer soil effect: theory and program implementation. *Chin J Comput Mech* 2012;29(4):582–8. [in Chinese].
- Liu GH, Lian JJ, Liang C, Zhao M. An effective approach for simulating multi-support earthquake underground motions. *Bull Earthq Eng* 2017;15(11):4635–59.
- Lou L, Zerva A. Effects of spatially variable ground motions on the seismic response of s skewed, multi-span, RC highway bridge. *Soil Dyn Earthq Eng* 2005;25(7):729–40.

- [31] Lunedei E, Albarello D. Power spectral density function and spatial autocorrelation of the ambient vibration full-wavefield generated by a distribution of spatially correlated surface sources. *Geophys J Int* 2016;204(3):1817–37.
- [32] Mott G. Reflection and refraction coefficients at a fluid-solid interface. *J Acoust Soc Am* 1971;50(3B):819–29.
- [33] Saxena V, Deodatis G, Shinozuka M. Effect of spatial variation of earthquake ground motion on the nonlinear dynamic response of highway bridges. In: *Proceedings of the 12th world conference on earthquake engineering*. Paper 2227; 2000.
- [34] Shrestha B, Hao H, Bi K. Effectiveness of using rubber bumper and restrainer on mitigating pounding and unseating damage of bridge structures subjected to spatially varying ground motions. *Eng Struct* 2014;79:195–210.
- [35] Tajimi H. A statistical method of determining the maximum response of a building structure during an earthquake. In: *Proceedings of the 2nd world conference on earthquake engineering*, Tokyo, Japan; 1960; 781–97.
- [36] The Report of the geological exploration in Tianjin. The Tianjin Institute of Geotechnical Investigation Surveying, Tianjin, China. (in Chinese); 2015.
- [37] Tian Li. Seismic response of power transmission tower-line system under multi-component multi-support excitations. *J Earthq Tsunami* 2012;6(4):389–96.
- [38] Wang S, Hao H. Effects of random variations of soil properties on site amplification of seismic ground motions. *Soil Dyn Earthq Eng* 2002;22(7):551–64.
- [39] Yan X, Yu HT, Yuan Y, Yuan JY. Multi-point shaking table test of the free field under non-uniform earthquake excitation. *Soils Found* 2015;55(5):985–1000.
- [40] Yang J, Sato T. Effects of pore-water saturation on seismic reflection and transmission from a boundary of porous soils. *Bull Seismol Soc Am* 2000;90(5):1313–7.
- [41] Yuan Y, Yu HT, Li C, Yan X, Yuan JY. Multi-point shaking table test for long tunnels subjected to non-uniform seismic loadings - Part I: theory and validation. *Soil Dyn Earthq Eng* 2018;108:177–86.
- [42] Yu HT, Cai C, Guan XF, Yuan Y. Analytical solution for long lined tunnels subjected to travelling loads. *Tunn Undergr Space Technol* 2016;58:209–15.
- [43] Yu HT, Yan X, Bobet A, Yuan Y, Xu GP, Su QK. Multi-point shaking table test of a long tunnel subjected to non-uniform seismic loadings. *Bull Earthq Eng* 2018;16(2):1041–59.
- [44] Yu HT, Yuan Y, Xu GP, Su QK, Yan X, Li C. Multi-point shaking table test for long tunnels subjected to non-uniform seismic loadings - Part II: application to the HZM immersed tunnel. *Soil Dyn Earthq Eng* 2018;108:187–95.
- [45] Zentner I, Poirion F. Enrichment of seismic ground motion databases using Karhunen–Loève expansion. *Earthq Eng Struct Dyn* 2012;41(14):1945–57.
- [46] Zerva A, Zervas V. Spatial variation of seismic ground motions: an overview. *Appl Mech Rev* 2002;55(3):271–97.
- [47] Zhao CG, Gao FP, Zeng QL. The reflection and transmission of plane waves on an interface between solid and liquid-filled porous solid with dissipation of energy. *Chin J Rock Mech Eng* 1996;15:470–5. [in Chinese].
- [48] Zhang N, Xia H, Roeck GD. Dynamic analysis of a train-bridge system under multi-support seismic excitations. *J Mech Sci Technol* 2010;24(11):2181–8.
- [49] Yu HT, Yang YS, Yuan Y. Analytical solution for a finite Euler-Bernoulli beam with single discontinuity in section under arbitrary dynamic loads. *Appl Math Model* 2018;60:571–80.
- [50] Yu HT, Zhang ZW, Chen JT, Bobet A, Zhao M, Yuan Y. Analytical solution for longitudinal seismic response of tunnel liners with sharp stiffness transition. *Tunn Undergr Space Technol* 2018;77:103–14.